ARTICLE

Nano-Photoelectrochemical Cell Arrays with Spatially Isolated Oxidation and Reduction Channels

Hang-Ah Park,[†] Siyuan Liu,[†] Youngseok Oh, Paul A. Salvador, Gregory S. Rohrer,[ID] and Mohammad F. Islam*[ID]

Department of Materials Science and Engineering, Carnegie Mellon University, 5000 Forbes Avenue, Pittsburgh, Pennsylvania 15213-3890, United States

S *Supporting Information*

ABSTRACT: Photoelectrochemical conversion of solar energy is explored for many diverse applications but suffers from poor efficiencies due to limited solar absorption, inadequate charge carrier separation, redox half-reactions occurring in close proximity, and/or long ion diffusion lengths. We have taken a drastically different approach to the design of photoelectrochemical cells (PECs) to spatially isolate reaction sites at the nanoscale to different materials and flow channels, suppressing carrier recombination and back-reaction of intermediates while shortening ion diffusion paths and, importantly, avoiding mixed product generation. We developed massively parallel nano-PECs composed of an array of open-ended carbon nanotubes (CNTs) with photoanodic reactions occurring on the outer walls, uniformly coated with titanium dioxide (TiO_2), and photocathodic reactions occurring on the inner walls, decorated with platinum (Pt). We verified the redox reaction isolation by demonstrating selective photodeposition of manganese oxide on the outside and silver on the inside of the TiO_2/CNT/Pt nanotubes. Further, the nano-PECs exhibit improved solar absorption and efficient charge transfer of photogenerated carriers to their respective redox sites, leading to a 1.8% photon-to-current conversion efficiency (a current density of 4.2 mA/cm^2) under white-light irradiation. The design principles demonstrated can be readily adapted to myriads of photocatalysts for cost-effective solar utilization.

KEYWORDS: *photoelectrochemical cell, photocatalyst, TiO_2, carbon nanotubes, water splitting*
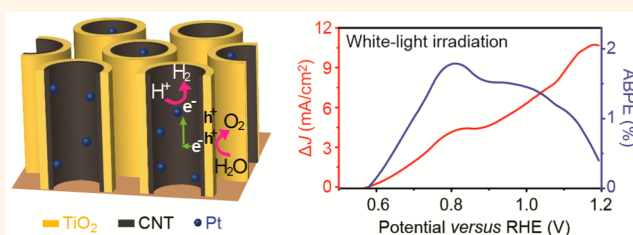
Photoelectrochemical conversion of solar energy has been extensively evaluated for energy generation, environmental remediation, and biological applications.[1] In the most widely explored approach, particulate photocatalysts composed of metal oxides and noble metals are used, often supported on carbon allotropes including micrometer-sized carbon particles, carbon nanotubes (CNTs), and graphene.[2–15] Benefits of this approach include relatively low cost for large-scale production, moderate catalytic surface area, reasonable charge separation, and negligible ion diffusion distances.[1–15] Unfortunately, known photocatalysts are either too costly or too inefficient due to limited solar absorption, inadequate charge carrier separation, and redox half-reactions occurring in close proximity that allow recombination of carriers and intermediates.[8,16–20] For hydrogen generation, confinement of reactions to separate flow channels is advantageous because it isolates the photogenerated gases and eliminates subsequent expensive separation steps.[16] Consequently, research has focused on the development of photocatalysts with appropriate intrinsic electronic structures, or complexed with photo-

sensitizers, to absorb a significant portion of the solar spectrum at energy levels appropriate to relevant photochemical reactions that occur at spatially separate locations. Useful photocatalysts must also be stable in a broad range of application environments and amenable to industrial-scale production at low cost. No known photocatalyst, however, possesses all these properties simultaneously.[1–20]

An alternate energy conversion approach is to use macroscale photoelectrochemical cells (PECs), in which the reactions occur at macroscopically isolated electrodes immersed in an aqueous electrolyte that is partitioned to isolate the electrodes and products while the electrodes are connected electrically *via* an external circuit.[21–23] Typically, one or both of these electrodes are photoactive, fabricated by coating conducting substrates with photocatalysts.[24] The thickness of photocatalyst layers is less than or equal to the diffusion length of

photogenerated carriers to minimize carrier recombination.[21−24] Aside from challenges associated with photocatalysts mentioned above, this class of PECs suffers from unacceptably high cost or poor overall efficiencies, the latter due to the limited photocatalyst thickness, poor solar absorption, low catalytic surface area, and long ion diffusion paths arising from the large physical separation between the electrodes.[24,25] Depositing catalysts directly on opposite sides of a conducting substrate and imparting nanostructured morphologies to the catalysts have not significantly improved the photocatalytic performance of such PECs.[24,26,27] Radical improvements in material properties and design principles that combine the prime strength of PECs, which is the spatial isolation of redox half-reactions and products, with benefits of particulate photocatalysts, especially short ion diffusion lengths and high catalytic surface area, are needed to realize efficient and economically competitive photoelectrochemical energy conversion.

Herein, we report on the fabrication of massively parallel nano-PECs composed of open-ended CNT arrays with oxide photocatalysts on the outside and metal cocatalysts on the inside of each CNT. The nano-PEC design isolates oxidation and reduction sites on the nanoscale to different materials and separate flow channels, incorporating the strengths of macro-scale PECs, while the short ion diffusion distances in the nano-PEC arrays overcome their geometrical issues. Further, oxide−CNT bonding offers improved solar absorption and direct carrier separation, the geometry of individual CNTs leads to short carrier diffusion lengths, and the massively parallel arrays lead to very high surface areas and strong overall light absorption, incorporating attractive features of particulate catalysts into PECs. We chose titanium dioxide (TiO_2) as the photocatalyst and platinum (Pt) as the cocatalyst in these nano-PECs because they are widely studied reference materials. We fabricate nano-PEC arrays using standard solution methods, characterize their microstructure using electron microscopy and by measuring their specific surface areas (SSA), evaluate the nature and number of bonds between TiO_2 and CNTs with Raman spectroscopy and XPS, and determine their photoelectrochemical properties through dye degradation and photocurrent measurements. Finally, we establish complete spatial isolation, over the nanoscale, of the oxidation and reduction reaction sites to separate flow channels by demonstrating selective photodeposition of manganese oxide (MnO_x) and silver (Ag) outside and inside the TiO_2/CNT/Pt nanotubes, respectively. Our results elucidate the design principles for nano-PECs that isolate redox reactions at the nanoscale and govern photoanodic performance in nano-PECs, leading to one of the best reported photochemical efficiencies for any photocatalyst and providing a clear path toward their further optimization.

RESULTS AND DISCUSSION

The major steps in the fabrication of TiO_2/CNT/Pt nano-PEC arrays are schematically shown in Figure 1. Similar routes were followed to fabricate partial cells, such as TiO_2/CNT arrays. We began by coating the inner walls of the 200 nm diameter cylindrical pores in anodic aluminum oxide (AAO) membranes (Figure 1A) with amorphous-TiO_2, via slow hydrolysis of titanium butoxide (Figure 1B), which was followed by deposition of a glucose layer on top of TiO_2 (Figure 1C). Next, we simultaneously crystallized TiO_2 and transformed the glucose layer into CNTs through pyrolysis of the AAO/
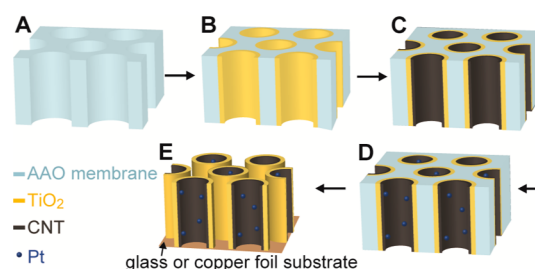

Figure 1. Schematic representation of the fabrication process for TiO_2/CNT/Pt membrane based nano-PEC arrays. (A) Anodized aluminum oxide (AAO) membranes with cylindrical pores of diameter ∼200 nm were used as a scaffold to synthesize coaxial (B) TiO_2 nanotubes on the outer wall of (C) CNTs. (D) Pt nanoparticles were then deposited on the inside of the interior wall of the CNTs. (E) AAO/TiO_2/CNT/Pt membrane structures were then attached either to a glass substrate using double-sided tape for experiments involving photodegradation of methylene blue dyes or to a copper foil using silver paste for photocurrent measurements. Finally, AAO was dissolved away to obtain the TiO_2/CNT/Pt membrane based nano-PEC arrays.

amorphous-TiO_2/glucose composites at 600 °C in argon. We then synthesized Pt nanoparticles inside the CNTs via reduction of hexachloroplatinic acid (Figure 1D). Finally, AAO was dissolved away using sodium hydroxide to obtain TiO_2/CNT/Pt membranes (Figure 1E) with photocatalysts TiO_2 spatially isolated from cocatalysts Pt at the nanoscale and connected via electrically conducting CNTs. These membranes have a density of ∼43.2 mg/mL with a TiO_2:CNT:Pt mass ratio of 90:7.5:2.5, which we corroborated by measuring the TiO_2:CNT mass ratio in TiO_2/CNT membranes, in which case the ratio was 92:8, using a thermal gravimetric analysis (TGA) technique (Figure S1).

We characterized the microstructure of the TiO_2/CNT/Pt membranes using scanning and transmission electron microscopy imaging (SEM and TEM, respectively) and by measuring the SSA and the pore size distributions using Brunauer−Emmet−Teller (BET) and Barrett−Joyner−Halenda (BJH) methods.[28,29] High-resolution SEM images show that the nano-PEC arrays indeed have a membrane like structure composed of tubes with highly uniform diameters of ∼200 nm (Figure 2A). Conventional-resolution TEM images confirm the average diameter of the tubes and further show uniform ∼10 nm thick TiO_2 on the outside and sparsely distributed ∼5 nm Pt nanoparticles on the inside of the innermost walls of CNTs (Figure 2B and its inset). High-resolution TEM images of a TiO_2/CNT/Pt nanotube corroborate the Pt nanoparticle sizes and TiO_2 thickness (Figure 2C and Figure S2), and corresponding diffraction patterns show that TiO_2 is anatase (inset of Figure 2C). Finally, the images also show that the CNTs had 3−5 walls with reasonable graphitic structure (Figure 2C), but the walls are not continuous, concentric graphene sheets that are typical of multiwall CNTs. The TiO_2/CNT membranes possess an SSA of 40 m²/g, calculated from measured adsorption data shown in Figure S3A, with nearly all pores having diameters of ≤3.5 nm (Figure S3B), likely a measure of the roughness of the outer surface of TiO_2 and the innermost wall of CNTs because the measurement is not capable of identifying the TiO_2/CNT nanotube diameter.

Because the TiO_2−CNT heterojunction affects carrier transfer and solar absorption, and defects in CNTs impact carrier transport, we characterized interactions between TiO_2
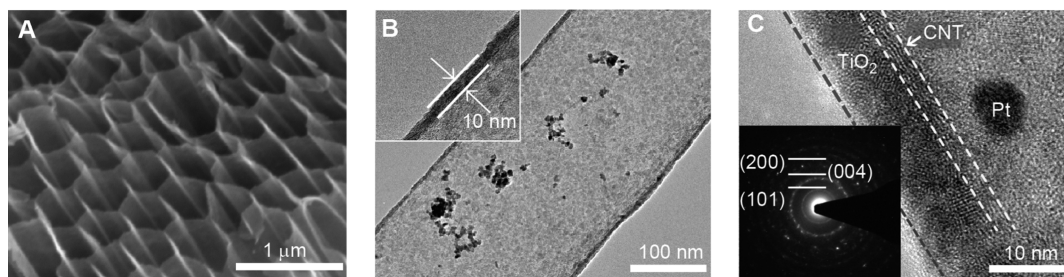
Figure 2. Morphology and microstructure of TiO$_2$/CNT/Pt nano-PEC arrays. (A) SEM images confirm that the nano-PECs indeed have a membrane geometry composed of nanotubular arrays. (B) Conventional-resolution TEM images show that each nanotube consists of a CNT with the outer wall coated with ~10 nm thick TiO$_2$ (shown in inset) and sparsely distributed Pt nanoparticles on the interior wall. (C) High-resolution TEM imaging of the TiO$_2$ layer and a corresponding diffraction pattern show that TiO$_2$ is anatase. Additionally, the TEM images show that the CNT walls have 3−5 graphene layers and Pt nanoparticles have diameters of ~5 nm. Note that the graphene layers are not continuous and concentric, which are typical of multiwall CNTs.

and CNTs as well as the structural integrity of CNTs in the TiO$_2$/CNT/Pt membranes using Raman spectroscopy (Figure 3) and compared them with anatase-TiO$_2$ membranes. The
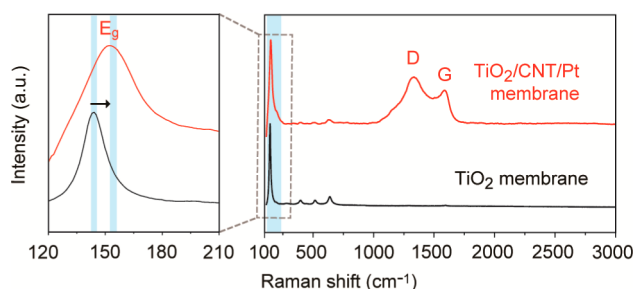

Figure 3. Raman spectra from TiO$_2$/CNT/Pt and anatase-TiO$_2$ membranes.

anatase-TiO$_2$ membranes were fabricated using the same AAO scaffolds and chemical reagents with identical reagent concentrations and reaction conditions with those used to synthesize TiO$_2$/CNT/Pt membranes. However, the anatase-TiO$_2$ membranes were annealed at 450 °C in air, because we found that amorphous-TiO$_2$, without being confined between CNTs and AAO, transformed into a mixture of anatase and rutile crystalline phases when heated to 600 °C in air. The Raman spectra from TiO$_2$/CNT membranes display distinct features associated with anatase-TiO$_2$ as well as CNTs. The characteristic E$_g$ mode associated with anatase-TiO$_2$ is blue-shifted by 7 cm^{-1} from 144 cm^{-1} for anatase-TiO$_2$ membranes to 151 cm^{-1} for TiO$_2$/CNT/Pt membranes, indicating strong interactions between TiO$_2$ and CNTs, presumably at the interface.[30] The Raman intensity ratio I_D/I_G between the CNT

D-band at ~1320 cm^{-1} and the G-band at ~1580 cm^{-1} characterizes structural defects in CNTs, with values of ~0.1 signifying highly defect-free CNTs and >1 indicating substantially defective CNTs.[15,31] Note, the D-band characterizes the sp^3-hybridized carbon, and the G-band quantifies the sp^2-hybridized carbon in CNTs.[31] The I_D/I_G for the TiO$_2$/CNT membrane is 1.34, indicating that CNTs have extensive defects, likely because the 600 °C pyrolysis temperature was well below the more suitable 800−950 °C that yields highly graphitic structures from glucose.[32] Removal of these defects provides a straightforward path for improving photocatalytic performance of TiO$_2$/CNT/Pt membranes.

We further evaluated TiO$_2$−CNT heterojunctions by examining bonding interactions between TiO$_2$ and CNTs by analyzing the carbon (C) 1s, titanium (Ti) 2p, and oxygen (O) 1s core level spectra measured using X-ray photoelectron spectroscopy (XPS). Deconvolving of the C 1s spectrum leads to five peaks with two dominant peaks at 283.6 and 284.7 eV arising from the C=C and the C−C bonds of the CNTs, respectively (Figure 4A). The third largest peak at 286.6 eV represents C−O bonds, suggesting that oxygen from some TiO$_2$ formed bonds with CNTs and/or the presence of CO groups at defects on CNTs. The last two peaks at 282.0 and 288.5 eV are respectively from Ti−C and Ti−O−C bonds, further validating that bonding occurs between TiO$_2$ and CNTs. Signatures of these bonds are present in the deconvolved Ti 2p spectrum (Figure 4B). The primary 2p$_{3/2}$ and 2p$_{1/2}$ peaks at 458.4 and 464.1 eV, respectively, result from the Ti−O (Ti^{4+}) bonds. Peaks associated with Ti−C bonds are located at 459.8 and 465.5 eV, while peaks related to Ti−O−C bonds are observed at 457.6 and 462.2 eV. Finally, the O 1s spectrum can be fitted into two peaks at 530.8 and 532.6 eV
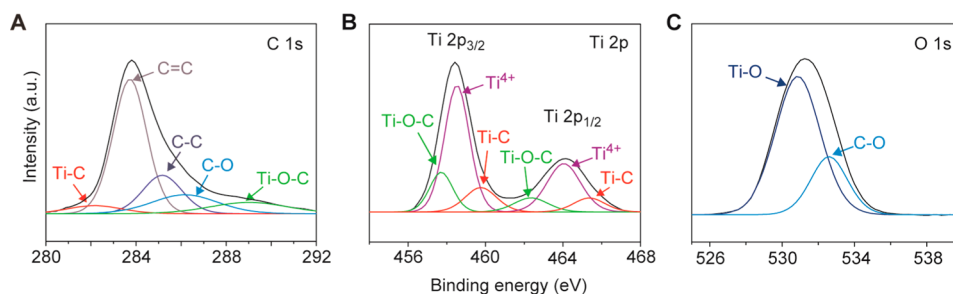

Figure 4. XPS spectra from TiO$_2$/CNT membranes for (A) C 1s, (B) Ti 2p, and (C) O 1s strongly suggest Ti−C and Ti−O−C bonds between TiO$_2$ and CNTs.

that can be attributed to Ti−O and C−O bonds, respectively (Figure 4C). The Ti−C and Ti−O−C bonds between TiO$_2$ and CNTs should facilitate fast electron transfer into CNTs, leading to a reduction in photogenerated carrier recombination and an enhancement in photocatalytic efficiency of the TiO$_2$/CNT/Pt membranes.

Since the Ti−C and Ti−O−C bonds exhibit broad optical absorbance,[33] they should also act as visible-light sensitizers for photoactivity. The optical absorbance properties of the anatase-TiO$_2$, CNT, and TiO$_2$/CNT membranes, measured using ultraviolet (UV)−visible reflectance spectroscopy, are shown in Figure 5. Anatase-TiO$_2$ membranes show a significant
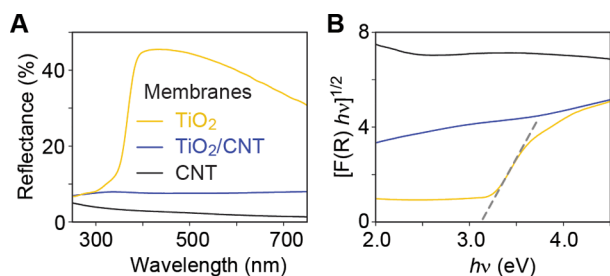

Figure 5. Optical absorbance properties of TiO$_2$, CNT, and TiO$_2$/CNT membranes. (A) Reflectance *versus* wavelength. (B) Tauc plot of $[F(R)h\nu]^{1/2}$ *versus* photon energy ($h\nu$) to estimate the band gap or absorption edge of TiO$_2$/CNT membranes.

reflectance across the visible spectrum, whereas the CNT and TiO$_2$/CNT membranes show minimal but broad reflectance over the same range (Figure 5A). The band gap and absorption band edge of materials are often estimated from Tauc plots, which involve plotting $[F(R)h\nu]^{1/2}$ *versus* photon energy ($h\nu$) and are generated from the reflectance measurements.[15,34,35] To this end, the Kubelka−Munk function, $F(R)$, was first calculated from the reflectance (R) using the expression $F(R) = (1 − R)^2/2R$, and then $[F(R)h\nu]^{1/2}$ was plotted as a function of $h\nu$ (Figure 5B).[36,37] Using this method, the band gap of the anatase-TiO$_2$ membranes is observed near the expected value of ∼3.2 eV.[38] Unfortunately, neither the CNT membranes nor the TiO$_2$/CNT membranes show a characteristic band gap or absorption edge, but rather a broad absorbance in the visible spectrum. Further, strong light absorbance by CNTs across the visible range prohibits unambiguous determination of contributions from the Ti−C and Ti−O−C bonds to the absorbance characteristics of TiO$_2$/CNT/Pt membranes, but the photosensitizing effects of these bonds are captured in visible-light photoactivity described below.

We began evaluation of the photoelectrochemical activity of TiO$_2$/CNT/Pt membranes by measuring methylene blue dye photodegradation over time under visible-light irradiation and by comparing its performance to similar measurements with dye alone, control samples (TiO$_2$, TiO$_2$/Pt, CNT, CNT/Pt, and TiO$_2$/CNT membranes), and literature reports. We first incubated all membranes in dye solution in the dark for dye adsorption on the membranes to reach equilibrium by monitoring the minimum elapsed time before the reduction in dye concentration plateaued, which was ∼2 h, as shown in Figure S4. Then we measured the dye concentration C as a function of light exposure or reaction time t (Figure S5). A common method to assess photocatalytic efficacy of PEC systems is *via* determination of the degradation rate constant, k, by plotting $\ln(C/C_0)$ *versus* t, as shown in Figure 6A, and fitting
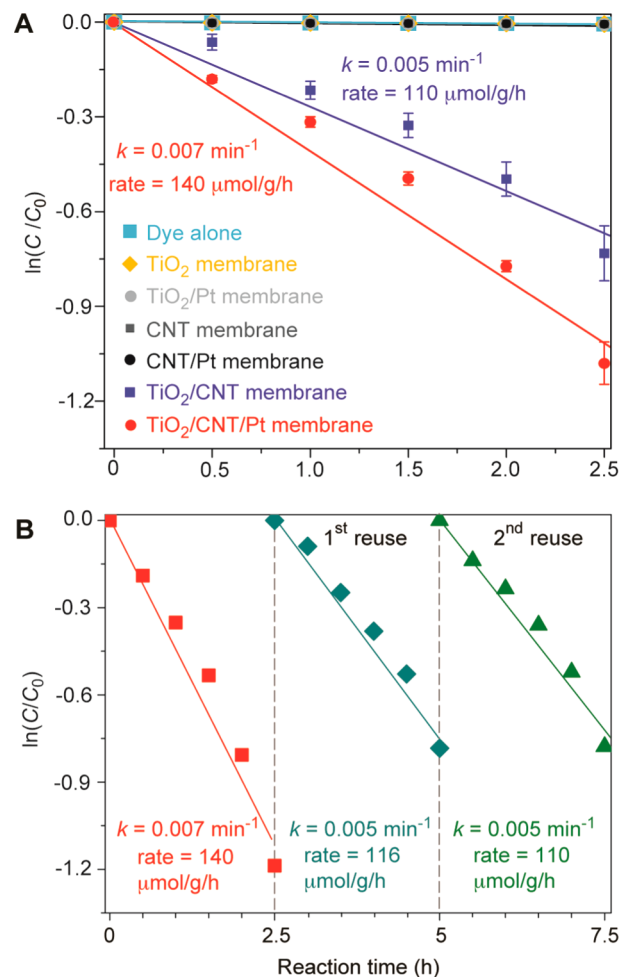

Figure 6. Photocatalytic methylene blue dye degradation and reusability of nano-PEC arrays. (A) Degradation rates and k for samples containing dye alone as well as membranes of TiO$_2$, TiO$_2$/Pt, CNT, CNT/Pt, TiO$_2$/CNT, and TiO$_2$/CNT/Pt under visible-light. (B) To test reusability, TiO$_2$/CNT/Pt membranes were rinsed in DI water after every 2.5 h of continuous use.

a pseudo-first-order model of the form $\ln(C/C_0) = −kt$, where C_0 is the dye concentration after adsorption equilibration.[5−15] TiO$_2$, TiO$_2$/Pt, CNT, and CNT/Pt membranes show negligible dye degradation capabilities with $k \approx 0$ min$^{−1}$, which is expected because TiO$_2$ is only photoactive in UV-light and CNTs are not known to generate photoactive carriers, even though they are strong light absorbers. In contrast, TiO$_2$/CNT/Pt membranes rapidly degrade dye in visible-light with $k \approx 7 \times 10^{−3}$ min$^{−1}$, likely because of the photosensitizing effects from the Ti−C and Ti−O−C bonds that extend carrier photogeneration in TiO$_2$ from UV- to visible-light. Interestingly, even the Pt-free TiO$_2$/CNT membranes degrade dyes reasonably rapidly, with $k \approx 5 \times 10^{−3}$ min$^{−1}$, likely due to the large electron-accepting capability of CNTs.

The k value of the TiO$_2$/CNT/Pt membrane is on the low end of k values when compared with other recently developed photocatalytic composites containing TiO$_2$ or superior photocatalysts with larger intrinsic solar absorption bandwidth, which are presented in Table S1 along with relevant experimental conditions, rate performances, and other characteristics.[6−10,12,14,15] We point out that k depends on the dye:photocatalyst molar ratio and can be readily increased by simply lowering this ratio. The ratios used in other experiments

are 1−2 orders of magnitude smaller than the ratio used in our experiments. To overcome this ambiguity, we also determined the dye decomposition amount by unit mass of the photocatalyst per unit time, *i.e.*, in units of μmol/g/h. Using this metric, the degradation rates for the $TiO_2/CNT/Pt$ and TiO_2/CNT membranes are respectively 140 ± 15 and 110 ± 8 μmol/g/h (all other membranes remain at ~0), which are 50% to 5 times greater than that of the same comparable composites (Table S1). Additionally, these membranes can be reused readily after cleaning by simply rinsing in deionized water. Under the same experimental conditions, including dye adsorption−desorption equilibration time, initial dye concentration, and dye:TiO_2 molar ratio, the degradation rate for $TiO_2/CNT/Pt$ membranes during the first reuse decreases by ~10% and then another ~5% during the second reuse (Figure 6B). We note that the residual dye concentration in the solution after dye adsorption−desorption (re)equilibration during the reuse cycles is successively slightly higher than that from the previous cycle, indicating sequentially lower dye adsorption, possibly due to incomplete dye removal during each rinsing cycle. Interestingly, the decrease in the degradation rates during reuse could be nearly eliminated through vigorous washing of the membranes. Unfortunately, such washing structurally damages the membranes including partially breaking off pieces of the membranes, which necessitates a reduction in dye solution volume to maintain the dye:TiO_2 molar ratio but in turn affects dye re-equilibration and degradation kinetics. Nevertheless, this observation corroborates that the decreases in degradation rates are likely due to incomplete cleaning of the membranes rather than from catalyst degradation.

These exceptional photodegradation rates are likely a reflection of the spatial isolation of photocatalysts and cocatalysts that promote carrier separation as well as reduce carrier recombination and back-reaction of the intermediates. We note that Pt addition to the interior walls of CNTs enhances the visible-light degradation rate only by ~20%, likely because only the Ti−C and Ti−O−C bonds are active during dye degradation in the visible-light and CNTs support sufficient carrier separation and reaction rates. Both k and the degradation rate of $TiO_2/CNT/Pt$ and TiO_2/CNT membranes improve under white-light illumination (Figure S6). Interestingly, the degradation rate for $TiO_2/CNT/Pt$ is 2-fold greater than that of TiO_2/CNT under white-light, an observation that is substantially different from that under visible-light (*cf.* Figure 6A with Figure S6). This is possibly because both the UV-active TiO_2 and visible-light-active Ti−C and Ti−O−C bonds photogenerate carriers under white-light and incorporation of Pt nanoparticles on CNTs improves the carrier separation and reduction reaction rates on the inside of the CNTs.

To evaluate fully their photoelectrochemical performance, we next characterized the photogenerated current densities of $TiO_2/CNT/Pt$ membranes in a 1 M sodium sulfate (Na_2SO_4) aqueous solution at pH 5.9 under both white- and visible-light illumination. A schematic illustration of the photocurrent measurement setup is shown in Figure 7A. Note that the inside of each coaxial $TiO_2/CNT/Pt$ nanotube was filled with poly(vinyl alcohol) (PVA) polymer prior to any photocurrent measurements to block contact between the electrolyte and the inner surfaces of CNTs or Pt. A comparison between SEM images of $TiO_2/CNT/Pt$ membranes before (Figure 2A) and after (Figure S7) filling the nanotubes with PVA polymer show that PVA successfully filled the nanotubes. Representative photocurrent density (*J*) *versus* potential (*V*) curves, plotted on
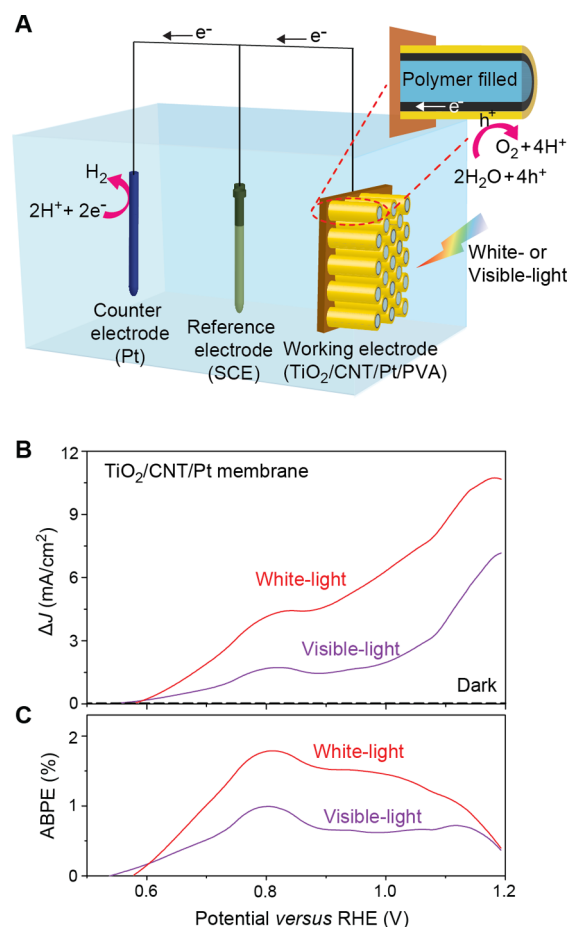

Figure 7. Photoelectrochemical performance of the nano-PEC arrays. (A) Schematic illustration of the experimental setup for photocurrent measurements. (B) $\Delta J−V$ curves of $TiO_2/CNT/Pt$ nano-PEC arrays measured in 1 M Na_2SO_4 electrolytes at pH 5.9 under white- and visible-light. Each nanotube was filled with polymer to prevent contact between CNTs or Pt with electrolyte. (C) Corresponding applied bias photon-to-current efficiency (ABPE) measured in a three-electrode configuration.

a reversible hydrogen electrode (RHE) scale, are shown in Figure S8. The $TiO_2/CNT/Pt$ membrane generates a substantial dark current density, likely from CNTs, but it is significantly smaller than J under white- and visible-light illumination. The net photocurrent densities (ΔJ), determined by subtracting the dark J values from the illuminated J values, are given in Figure 7B for the $TiO_2/CNT/Pt$ membrane. They exhibit an onset potential of ~0.3 V *versus* RHE, for both white- and visible-light, and generally rise with V up to 1.23 V *versus* RHE. TiO_2/CNT membranes show comparable $\Delta J−V$ curves (Figure S9), whereas TiO_2, TiO_2/Pt, CNT, and CNT/Pt membranes show negligible ΔJ (Figure S10). Since each coaxial nanotube was filled with PVA to prevent the inner walls from coming into contact with the electrolyte and participating in the cathodic reaction, it is reasonable that the $\Delta J−V$ curves of $TiO_2/CNT/Pt$ and TiO_2/CNT membranes are similar. Visible-light-generated photocurrent by $TiO_2/CNT/Pt$ and TiO_2/CNT membranes is an outcome of the photosensitizing effects of the Ti−C and Ti−O−C bonds on UV-light-active TiO_2. Furthermore, assuming that TiO_2 generates carriers under white-light illumination, the difference in ΔJ between TiO_2 and $TiO_2/CNT/Pt$ (or TiO_2/CNT) membranes (*cf.* Figure S10

with Figure 7B or Figure S9) indicates efficient electron transfer from TiO_2 to CNTs *via* the TiO_2−CNT heterojunction, possibly facilitated by the Ti−C and Ti−O−C bonds, leading to carrier recombination suppression in TiO_2. The absence of a plateau in $\Delta J–V$ curves for both TiO_2/CNT/Pt and TiO_2/CNT membranes can also originate from the same mechanism.

The applied bias photon-to-current efficiencies (ABPE) of TiO_2/CNT/Pt membranes under white- and visible-light, calculated from the $\Delta J–V$ curves, reach 1.8% and 1%, with corresponding ΔJ values of 4.2 and 1.7 mA/cm^2 at 0.8 V *versus* RHE, respectively (Figure 7C). These values are 3−50× larger than other recently developed TiO_2-based photocatalytic composites[39−42] and 2−6× greater than other leading photocatalysts with intrinsic visible-light activity;[43,44] these comparisons are tabulated in Table S2. Lastly, ΔJ, measured at a constant bias of 0.8 V *versus* RHE, of TiO_2/CNT/Pt membranes remains largely unchanged for 4 h (Figure 8), suggesting structural and functional stability of these membranes and TiO_2−CNT heterojunctions.
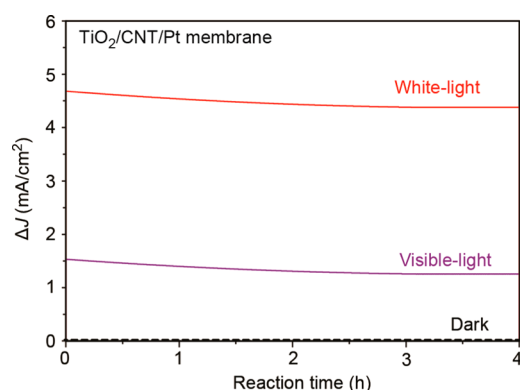

Figure 8. Photogenerated current density (ΔJ) *versus* time for TiO_2/CNT/Pt membranes under white- and visible-light in 1 M Na_2SO_4 electrolytes at pH 5.9.

In addition to the exceptional photoelectrochemical performance, a distinctive feature of the design of our TiO_2/CNT/Pt nano-PEC arrays is the complete spatial isolation of the oxidation and reduction reaction sites, over the nanoscale, to separate flow channels. We demonstrated this feature by first establishing the flow channel isolation and then demonstrating selective photodeposition of manganese oxide (MnO_x) and

silver (Ag) respectively outside and inside the TiO_2/CNT/Pt nanotubes. The nano-PEC arrays show negligible methylene blue dye degradation rates if AAO is retained (Figure 9A), which blocks the outer flow channel (TiO_2), but the inner flow channel (CNT/Pt) remains exposed, suggesting that the CNTs are largely pinhole-free. Note that large quantities of pinholes would allow access to the TiO_2 through the inner flow channel. To identify oxidation reaction sites, we added powdered TiO_2/CNT/Pt membranes in 10 mM manganese sulfate ($MnSO_4$) solution with 10 mM sodium iodate ($NaIO_3$), which scavenges electrons, and irradiated the mixture with visible-light for 30 min. Conventional-resolution TEM images of the membranes show that each TiO_2/CNT/Pt nanotube, which has a smooth outer wall surface, is covered with a thin layer of crystalline MnO_x flakes (*cf.* Figure 9B with Figure 2B) that protrude away from the nanotubes, strongly suggesting that the flakes are on the outer wall of the nanotubes and that the oxidation reaction occurred on the TiO_2 surface. Further, the lattice spacing in these flakes, determined from the high-resolution TEM images, is 0.29 nm, which matches well with the MnO_2 (001) plane (Figure S11A,B). Energy dispersive X-ray spectroscopy (EDS)-based elemental analysis shows ~8% Mn after 30 min of photodeposition, further corroborating the presence of Mn. We postulate that during visible-light irradiation photogenerated holes remain on the TiO_2 and oxidize Mn^{2+} solution species to insoluble solid products, which deposit on the outer walls, while electrons transfer to the inside of the TiO_2/CNT/Pt nanotubes and are scavenged by IO_3^-. The proposed mechanism is illustrated in Figure 9C.

We similarly verified the location of reduction sites by adding powdered TiO_2/CNT/Pt membranes into a 10 mM silver nitrate ($AgNO_3$) solution followed by 30 min of visible-light irradiation. Conventional-resolution TEM images show Ag nanoparticles, which are ~20 nm in diameter and which appear only after the photodeposition reaction, are distributed throughout the inside of the nanotubes. Ag nanoparticles are easily differentiable from Pt nanoparticles by their size; the Pt ones are much smaller, with diameters of 3−5 nm (*cf.* Figure 9D and Figure S11C with Figure 2B and C). The lattice spacing of these larger nanoparticles, resolved from the high-resolution TEM images, is 0.24 nm, which is similar to the Ag (111) plane (Figure S11D). Further, through TEM imaging of the TiO_2/CNT/Pt nanotube wall, we estimate that more than 91% of the Ag nanoparticles are located on the inner wall of CNTs and near or next to Pt nanoparticles (Figure S12A−F), where the
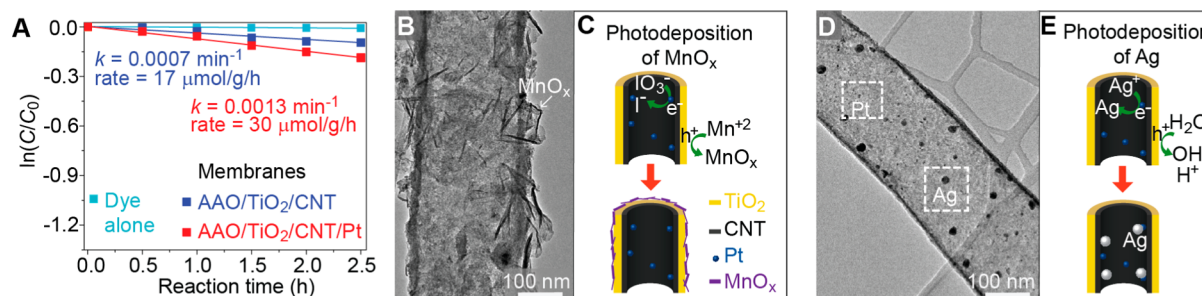

Figure 9. Verification of complete spatial isolation of oxidation and reduction sites by photodeposition of MnO_x and Ag. (A) Photocatalytic methylene blue dye degradation for samples containing dye alone as well as AAO/TiO_2/CNT and AAO/TiO_2/CNT/Pt membranes under visible-light. The negligible dye degradation rates for AAO/TiO_2/CNT/Pt and AAO/TiO_2/CNT membranes likely originate from exposed TiO_2 at the two membrane surfaces that are in contact with the dye solution. (B and D) Conventional-resolution TEM image of MnO_x on the outer wall surface and Ag in the inside of a TiO_2/CNT/Pt nanotube, respectively. Schematic illustration of proposed photodeposition mechanisms of (C) MnO_x and (E) Ag.

reduction reaction likely occurred. A few Ag nanoparticles on the outside of the nanotubes are likely an artifact of sample preparation for TEM imaging that involved dispersing TiO_2/CNT/Ag in ethanol using sonication and then spraying onto a TEM grid. Elemental analysis from EDS measurements shows ~10% Ag inside the TiO_2/CNT/Pt nanotubes after 30 min of photodeposition, further confirming Ag presence. We propose that during visible-light irradiation photogenerated electrons transfer to CNTs and/or Pt nanoparticles and reduce Ag^+ ions into Ag nanoparticles inside the nanotubes, and the holes are collected in TiO_2 and participate in water oxidation on the outside of the nanotubes, as illustrated in Figure 9E.

CONCLUSIONS

We have successfully fabricated massively parallel nano-PECs based on open-ended CNT arrays having photocatalysts coated over the outside wall, where the oxidation reaction occurs, and cocatalysts decorated onto the inside wall of each CNT, where reduction reaction occurs. This design scheme overcomes geometrical issues of macroscale PECs, spatially isolating oxidation and reduction sites at the nanoscale to different materials and separate flow channels, which we establish by selective photodeposition of MnO_x on the outside and Ag on the inside of the TiO_2/CNT/Pt nanotubes. Furthermore, the arrays improve on photocatalyst design, building in strong solar absorption, direct carrier separation, short diffusion paths, and high surface areas. The nano-PECs exhibit exceptional photoelectrochemical performance with an ABPE of 1.8% (1%), which corresponds to a ΔJ of 4.2 mA/cm^2 (1.7 mA/cm^2) under white-light (visible-light) irradiation, which is among the highest reported for any photocatalyst. This outstanding efficiency is achieved using highly defective CNTs, which hinder carrier transport to the cocatalyst, and a UV-active photocatalyst (TiO_2), which has limited solar absorption. Furthermore, these PECs have unoptimized interfacial bonding between the photocatalyst and CNTs that limits carrier transfer between them and visible-light sensitization of the photocatalyst. We believe that these shortcomings could be readily overcome by combining most highly performing photoanodic metal oxides, such as bismuth vanadate[45] or indium tantalate,[46] or metal oxynitrides with CNTs containing far fewer defects to vastly improve the photoelectrochemical performance while avoiding mixed product generation toward cost-effective solar energy conversion.

METHODS

Fabrication of TiO_2/CNT/Pt Membranes. *Synthesis of AAO/Amorphous-TiO_2 Membranes.* To coat uniformly and thinly the inner wall of the cylindrical pores of AAO membranes with TiO_2, we used a sol–gel method. Titanium butoxide (TBOT) was used as the Ti precursor and was dissolved in anhydrous ethanol (EtOH) under a nitrogen atmosphere at a TBOT:EtOH molar ratio of 1:100. The circular AAO membranes (Whatman) were 25 mm in diameter and 60 μm thick, and the cylindrical pores were 200 nm in diameter. The AAO membranes were soaked in 2 mL of the TBOT solution, inside a glass jar under low vacuum to facilitate TBOT infiltration into the pores of AAO membranes, until air bubbles stopped escaping from the membranes. TBOT was then slowly hydrolyzed by placing the glass jar, with AAO membranes immersed in the TBOT solution, inside a second larger glass jar containing 2 mL of deionized (DI) water (Ultrapure Milli-Q, resistivity 18.2 MΩ·cm). The larger jar was tightly capped such that water vapor from the larger glass jar could slowly hydrolyze the TBOT inside of the pores of AAO membranes in the smaller encapsulated jar. After 2.5 h of exposure, the AAO/TiO_2

membranes were removed, excess TiO_2 was scrapped off the outer surfaces, the membranes were washed with ethanol several times to remove unreacted TBOT, and they were dried in air at 60 °C for 12 h. TiO_2 that formed within the pores of the AAO membranes was amorphous.

Synthesis of AAO/TiO_2/CNT Membranes. To make coaxial CNTs inside each cylindrical pore, an AAO/amorphous-TiO_2 membrane was first soaked in 5 mL of an aqueous solution of 0.1 M glucose under low vacuum for ~1 h to remove any air bubbles trapped inside the membrane and to facilitate solution infiltration. The sample was then removed, and excess glucose was carefully scrapped off the outer surfaces. The sample was then dried at 60 °C for 3 h and then at 180 °C for 3 h. The glucose coating was performed twice. Subsequently, the amorphous-TiO_2 was crystallized and glucose was converted into CNTs simultaneously through pyrolysis of the AAO/amorphous-TiO_2/glucose membranes at 600 °C for 5 h in argon. Lastly, the sample surfaces were scraped carefully using a piece of soft polymer and washed off with anhydrous ethanol before drying at 60 °C for 12 h. We note that a higher pyrolysis temperature of 800−950 °C is required to make CNTs with fewer defects. However, we chose a lower temperature here to avoid transformation of TiO_2 into rutile, which has a lower photocatalytic activity than anatase, and coarsening of TiO_2, which would modify the thickness and uniformity of the oxide layer.

Synthesis of AAO/TiO_2/CNT/Pt Membranes. To isolate the TiO_2 photocatalyst on the outer wall of the CNT from the Pt cocatalysts, we synthesized Pt nanoparticles on the inner walls of the CNTs. Pyrolyzed AAO/TiO_2/CNT membranes were soaked in a 10 mM aqueous solution of hexachloroplatinic acid (H_2PtCl_6) under low vacuum for ~1 h to remove any air bubbles trapped inside the membranes and to facilitate solution infiltration. The samples were removed from H_2PtCl_6 solution and were gently wiped using a wet lint-free wipe (Kimwipes; Kimtech) to remove excess solution from the surfaces to prevent platinum from forming at the surfaces in the next step. To create Pt nanoparticles, the H_2PtCl_6 solution within the membranes was reduced by dropwise addition of 0.5 mL of a sodium borohydride ($NaBH_4$) solution, which was prepared by mixing 40 mM $NaBH_4$ with 20 mM sodium hydroxide (NaOH) solution. After ~30 min of reduction reaction, the sample was washed with DI water to remove unreacted H_2PtCl_6, $NaBH_4$, and NaOH solutions. The samples were subsequently dried at 60 °C for 12 h. The Pt deposition was performed twice to achieve sufficient Pt in the membranes.

Removal of AAO to Obtain TiO_2/CNT/Pt Membranes. To prepare membranes for methylene blue dye degradation and photocurrent generation experiments, the AAO/TiO_2/CNT/Pt membranes were respectively attached to glass slides (Thermo Scientific) using transparent double-sided tape and to copper foils using silver paste (Dupont 4929N) to retain the membrane geometry upon AAO removal. The samples were then immersed in a 2 M NaOH solution for 5 h at room temperature, with stirring, to dissolve AAO. They were then neutralized to pH 7 using DI water and dried at 60 °C for 12 h. To prepare powdered samples for experiments involving photodeposition of MnO_x and Ag, AAO/TiO_2/CNT/Pt membranes were soaked in a 2 M NaOH solution for 5 h, with stirring at room temperature, to dissolve AAO and to release TiO_2/CNT/Pt nanotubes. The samples were then washed with DI water until they reached pH 7, deposited on a filter paper, and dried at 60 °C for 12 h.

All membranes (*i.e.*, TiO_2, TiO_2/Pt, CNT, CNT/Pt, TiO_2/CNT, and TiO_2/CNT/Pt), whether attached to glass slides or copper tapes or in powdered form, were fabricated in dimensions of the starting AAO membrane dimensions (25 mm in diameter and 60 μm in thickness). We measured the masses of each type of membrane using a balance (XS205; Mettler Toledo) that has a resolution of 0.01 mg and calculated their average density. The average density of membranes: $TiO_2 \approx 38.7$ mg/mL, TiO_2/Pt ≈ 39.8 mg/mL, CNT ≈ 3.4 mg/mL, CNT/Pt ≈ 4.5 mg/mL, TiO_2/CNT ≈ 42.2 mg/mL, and TiO_2/CNT/Pt ≈ 43.2 mg/mL. Furthermore, by measuring the mass after every synthesis step, masses of TiO_2, CNT, and Pt in each type of membrane were also determined.

Sample Characterization. High-resolution SEM images were taken using an FEI Quanta 600. Conventional-resolution and high-resolution TEM images were collected using a Tecnai F20 at 200 kV and a FEI Titan 83 at 300 kV, respectively. Elemental analyses were performed with an ASPEX SEM equipped with an energy dispersive X-ray spectrometer. TGA measurements were carried out using a Q50 (TA Instrumentation) with specimens being heated at a rate of 5 °C/min under atmospheric air over a temperature range of 25 to 700 °C. The Raman spectra were collected using a Raman confocal microscope (inVia, Renishaw) with a 50×, 0.75 NA air objective (Leica Microsystems) and with a 785 nm (1.58 eV) laser. To avoid heat-induced damage to the samples, we used a laser power of 10 mW, a spot size of ~1–2 μm, and an exposure time of ~1 s. Five different locations were investigated for each sample, to verify uniformity, and at every location five scans were collected. The 25 scans were then averaged to improve the signal-to-noise ratio. Each Raman spectrum was normalized by its G-band intensity. Data collection and analysis were performed using WiRE software (Renishaw). The SSA of TiO_2/CNT membranes were determined from nitrogen adsorption and desorption measurements carried out with a surface area analyzer (Micromeritics Gemini VII 2390) at 77 K and calculated using the BET method.[28] The pore diameter ($2r$), pore volume (V), and pore diameter distributions (dV/dr) were calculated from the desorption branch of the isotherms using the BJH method.[29] The reflectance properties of the samples were measured using an OL 770-LED multichannel spectroradiometer that has a cold cathode mercury (Hg) vapor lamp as a light source and an integrating sphere. XPS data were collected with a DESA 150 analyzer (Staib instruments) using Al Kα X-rays as a probe, generated from a TX400/2 X-ray gun (PSP Vacuum Technology). Elemental analysis was carried out using CasaXPS. Concentrations of methylene blue dye solutions were measured using a Cary 5000 spectrometer (Varian).

Methylene Blue Dye Photodegradation. For these experiments, membranes attached to glass slides were cut into dimensions of 7 mm × 8 mm × 60 μm (length × width × thickness). The calculated total mass was based on the average densities. The mass of each component was determined from their mass ratios. Test samples were either 0.130 mg of TiO_2 membranes, 0.134 mg of TiO_2/Pt membranes (composed of 0.130 mg of TiO_2 and 0.004 mg of Pt), 0.011 mg of CNT membranes, 0.015 mg of CNT/Pt membranes (composed of 0.011 mg of CNT and 0.004 mg of Pt), 0.141 mg of TiO_2/CNT membranes (composed of 0.130 mg of TiO_2 and 0.011 mg of CNTs), or 0.145 mg of TiO_2/CNT/Pt membranes (composed of 0.130 mg of TiO_2, 0.011 mg of CNTs, and 0.004 mg of Pt).

To allow for dye solution infiltration into the membrane and equilibration of the dye with the photocatalyst, the test sample was soaked in 4 mL of an aqueous solution of 0.02 mM methylene blue, in a glass vial, for 2 h, in the dark, under vacuum, and with stirring using a magnetic stir bar. To confirm that the dye adsorption on the test sample equilibrated by the end of the 2 h soak, 0.5 mL of dye solution was periodically removed and its absorbance characterized. The dye concentration in solution measurably decreased after the 2 h equilibration soak; hence, in all dye degradation experiments, the value of C_0 corresponded to the value measured after the dye adsorption equilibration. For dye degradation experiments under visible-light, the equilibrated sample was irradiated with a 300 W Hg lamp (with a cooling system) that had a UV cutoff filter, which blocked light with wavelengths $\lambda < 420$ nm, and an infrared cutoff filter, which blocked light with $\lambda \geq 1200$ nm. We periodically measured the absorbance of the dye solution using a Varian Cary spectrometer by sampling 0.5 mL of the solution. The dye concentration C was determined from the absorbance at 665 nm, which is the maximum absorbance peak of the dye.

For reusability tests, we removed the test sample from the dye solution, rinsed it in DI water, and then soaked it in 0.02 mM dye solution in the dark for 2 h to achieve dye adsorption (re)equilibration. After the (re)equilibration soak, we measured the residual dye concentration in the solution to determine dye adsorption on test samples during the reuse cycles, which were slightly successively higher than that from the previous cycle, indicating sequentially lower dye

adsorption, possibly due to incomplete dye removal during each rinsing cycle. To maintain the same dye:TiO_2 molar ratio for all tests of dye degradation, we removed the test sample from the equilibration solution and submerged it in a dye solution with the same C_0 used in first degradation cycle.

Photocurrent Measurements. To fabricate photoanodes for photoelectrochemical investigations, the AAO/TiO_2/CNT/Pt membranes were attached to the copper foil with silver paste and were then cut into 3.5 mm × 6 mm × 60 μm (length × width × thickness) pieces, which corresponds to a total sample mass of 0.0544 mg and component masses of 0.0488 mg of TiO_2, 0.0042 mg of CNTs, and 0.0014 mg of Pt. To fill the inside of each TiO_2/CNT/Pt nanotube with PVA polymer, a test sample was soaked into 10 wt % PVA solution under vacuum for ~12 h to remove any air bubbles trapped inside the membrane and to facilitate solution infiltration. The sample was then removed from the solution and the surface was gently wiped with a wet Kimwipes wipe to remove excess PVA solution from the surface. Notice that the AAO hinders the PVA polymer from coating the outer surfaces of TiO_2. The sample was then dried for ~6 h, and the surface was wiped again with a wet Kimwipes wipe to remove any residual PVA. The copper foil and the silver paste around the membrane were coated with epoxy (3M) to prevent contact between the electrolyte and the silver paste or copper electrode. Finally, the AAO membrane was dissolved away by immersing the sample in a 2 M NaOH solution for 5 h at room temperature under stirring, neutralizing the solution to pH 7 using DI water, and drying at 60 °C for 12 h. Pt-free photoanodes were prepared using the same process but from TiO_2/CNT membranes (of the same dimensions as the Pt-containing membranes). The corresponding total sample mass was 0.0530 mg, and the component masses were 0.0488 mg of TiO_2 and 0.0042 mg of CNTs.

Photocurrent measurements of TiO_2/CNT/Pt and TiO_2/CNT membranes were made using a three-electrode configuration, with a saturated calomel electrode (SCE, Koslow) as a reference electrode, a coiled platinum wire (BAS, Japan) as a counter electrode, and the membrane as the working electrode. The electrolyte was a 1 M sodium sulfate (Na_2SO_4) aqueous solution at pH 5.9. A 150 W xenon lamp was used as the light source and had a UV cutoff filter ($\lambda < 420$ nm) and an infrared cutoff filter ($\lambda \geq 1200$ nm), which was tuned to provide a power density at the plane of the sample of 100 mW/cm^2 under white-light illumination and 73 mW/cm^2 under visible-light illumination. The electrodes were swept from negative to positive potentials at a scan rate of 10 mV/s using an SP-200 potentiostat (BioLogic Science Instrument). We converted the J−V measurements on the SCE scale to the RHE scale to facilitate comparison to the water splitting potential levels using the following relationship:[43]
Potential *versus* RHE = potential *versus* SCE + 0.244 + 0.0591 V × pH.

The applied bias photon-to-current efficiency was calculated using the expression[43] ABPE% = ΔJ [mA/cm^2] × (1.23 − V_{bias}) [V] × 100/P_{in}, where ΔJ is the net photocurrent density after subtracting dark current, V_{bias} is the applied bias between the photoanode and the reference electrode on the RHE scale, and P_{in} is the power density of incident light. Note that the expression assumes a Faradaic efficiency of 100%.

Photodeposition of MnO$_x$ and Ag on TiO_2/CNT/Pt Membranes. *Photodeposition of MnO$_x$.* The sample for photodeposition of MnO$_x$ on TiO_2/CNT/Pt membranes was prepared by adding 0.5 mg of powdered TiO_2/CNT/Pt membranes to 2 mL of a solution of 10 mM manganese sulfate (MnSO$_4$) and 10 mM sodium iodate (NaIO$_3$), which scavenges electrons. The sample was then irradiated with visible-light for 30 min. The light source was a 300 W Hg lamp with a UV cutoff filter ($\lambda < 420$ nm) and an infrared cutoff filter ($\lambda \geq 1200$ nm). Finally, the sample was washed with DI water to remove unreacted reagents, centrifuged at 21000g to sediment the sample, and dried in air at room temperature.

Photodeposition of Ag. The sample for photodeposition of Ag on TiO_2/CNT/Pt membranes was prepared by adding 0.5 mg of powdered TiO_2/CNT/Pt membranes to 2 mL of a 10 mM aqueous silver nitrate (AgNO$_3$) solution, where water acted as the hole scavenger. The sample was then irradiated with visible-light for 30 min.

The light source and the final processing steps were the same as those used for MnOₓ photodeposition.

All photodegradation of dye experiments, photocurrent generation measurements, and MnOₓ and Ag deposition at each condition were repeated with at least three different samples.

ASSOCIATED CONTENT

Ⓢ Supporting Information

The Supporting Information is available free of charge on the ACS Publications website at DOI: 10.1021/acsnano.6b08387.

Figures of (1) TGA of TiO_2/CNT membrane, (2) high-resolution TEM image of TiO_2/CNT/Pt membranes, (3) adsorption isotherms and pore characteristics of TiO_2/CNT membranes, (4) adsorption−desorption equilibration time of methylene blue dye on TiO_2/CNT/Pt and TiO_2/CNT membranes in the dark, (5) dye absorption spectra at various reaction time intervals, (6) photocatalytic methylene blue dye degradation of TiO_2/CNT and TiO_2/CNT/Pt membrane under white-light, (7) SEM image of TiO_2/CNT/Pt membrane after being filled with PVA polymer, (8) $J−V$ curves of TiO_2/CNT/Pt membrane on the RHE scale, (9) $\Delta J−V$ curves on an RHE scale for TiO_2/CNT membranes under white- and visible-light, (10) $\Delta J−V$ curves on an RHE scale by TiO_2, TiO_2/Pt, CNT, CNT/Pt membranes under white- and visible-light, (11) TEM images of MnOₓ flakes on the outer wall surface and Ag nanoparticles on the inside of TiO_2/CNT/Pt nanotubes, and (12) conventional-resolution TEM images of photodeposited Ag nanoparticles on the interior CNT wall of TiO_2/CNT/Pt membranes (PDF)

AUTHOR INFORMATION

Corresponding Author

*E-mail: mohammad@cmu.edu.

ORCID Ⓘ

Gregory S. Rohrer: 0000-0002-9671-3034
Mohammad F. Islam: 0000-0001-9253-3709

Author Contributions

†H.-A. Park and S. Liu contributed equally. M.F.I., P.A.S., and G.S.R. conceived the project. H-A.P. and S.L. carried out the measurements under supervision of P.A.S. G.S.R. and M.F.I. Y.O. performed preliminary experiments. All authors participated in writing the manuscript and have given approval to the final version of the manuscript.

Notes

The authors declare no competing financial interest.

REFERENCES

(1) Chen, X. B.; Shen, S. H.; Guo, L. J.; Mao, S. S. Semiconductor-Based Photocatalytic Hydrogen Generation. *Chem. Rev.* **2010**, *110*, 6503−6570.

(2) Li, R. G.; Zhang, F. X.; Wang, D. G.; Yang, J. X.; Li, M. R.; Zhu, J.; Zhou, X.; Han, H. X.; Li, C. Spatial Separation of Photogenerated Electrons and Holes Among {010} and {110} Crystal Facets of BiVO₄. *Nat. Commun.* **2013**, *4*, 1432.

(3) Liu, S. X.; Qu, Z. P.; Han, X. W.; Sun, C. L. A Mechanism for Enhanced Photocatalytic Activity of Silver-Loaded Titanium Dioxide. *Catal. Today* **2004**, *93−5*, 877−884.

(4) Subramanian, V.; Wolf, E. E.; Kamat, P. V. Catalysis with TiO_2/Gold Nanocomposites. Effect of Metal Particle Size on the Fermi Level Equilibration. *J. Am. Chem. Soc.* **2004**, *126*, 4943−4950.

(5) An, C. H.; Peng, S. N.; Sun, Y. G. Facile Synthesis of Sunlight-Driven AgCl:Ag Plasmonic Nanophotocatalyst. *Adv. Mater.* **2010**, *22*, 2570−2574.

(6) Bai, X. J.; Wang, L.; Zhu, Y. F. Visible Photocatalytic Activity Enhancement of ZnWO₄ by Graphene Hybridization. *ACS Catal.* **2012**, *2*, 2769−2778.

(7) Chen, Z.; Li, D.; Zhan, W.; Shao, Y.; Chen, T.; Sun, M.; Fu, X. Photocatalytic Degradation of Dyes by ZnIn₂S₄ Microspheres Under Visible Light Irradiation. *J. Phys. Chem. C* **2009**, *113*, 4433−4440.

(8) Cui, G. W.; Wang, W. L.; Ma, M. Y.; Zhang, M.; Xia, X. Y.; Han, F. Y.; Shi, X. F.; Zhao, Y. Q.; Dong, Y. B.; Tang, B. Rational Design of Carbon and TiO_2 Assembly Materials: Covered or Strewn, Which is Better for Photocatalysis? *Chem. Commun.* **2013**, *49*, 6415−6417.

(9) Djokic, V. R.; Marinkovic, A. D.; Ersen, O.; Uskokovic, P. S.; Petrovic, R. D.; Radmilovic, V. L. R.; Janackovic, D. T. The Dependence of the Photocatalytic Activity of TiO_2/Carbon Nanotubes Nanocomposites on the Modification of the Carbon Nanotubes. *Ceram. Int.* **2014**, *40*, 4009−4018.

(10) Lee, W. J.; Lee, J. M.; Kochuveedu, S. T.; Han, T. H.; Jeong, H. Y.; Park, M.; Yun, J. M.; Kwon, J.; No, K.; Kim, D. H.; Kim, S. O. Biomineralized N-doped CNT/TiO_2 Core/Shell Nanowires for Visible Light Photocatalysis. *ACS Nano* **2012**, *6*, 935−943.

(11) Soni, S. S.; Henderson, M. J.; Bardeau, J. F.; Gibaud, A. Visible-Light Photocatalysis in Titania-Based Mesoporous Thin Films. *Adv. Mater.* **2008**, *20*, 1493−1498.

(12) Xing, M.; Li, X.; Zhang, J. Synergistic Effect on the Visible Light Activity of Ti^{3+} Doped TiO_2 Nanorods/Boron Doped Graphene Composite. *Sci. Rep.* **2014**, *4*, 5493.

(13) Yang, N. L.; Liu, Y. Y.; Wen, H.; Tang, Z. Y.; Zhao, H. J.; Li, Y. L.; Wang, D. Photocatalytic Properties of Graphdiyne and Graphene Modified TiO_2: from Theory to Experiment. *ACS Nano* **2013**, *7*, 1504−1512.

(14) Zhang, H.; Lv, X. J.; Li, Y. M.; Wang, Y.; Li, J. H. P25-Graphene Composite as a High Performance Photocatalyst. *ACS Nano* **2010**, *4*, 380−386.

(15) Park, H.-A.; Liu, S.; Salvador, P. A.; Rohrer, G. S.; Islam, M. F. High Visible-Light Photochemical Activity of Titania Decorated on Single-Wall Carbon Nanotube Aerogels. *RSC Adv.* **2016**, *6*, 22285−22294.

(16) Maeda, K.; Domen, K. Photocatalytic Water Splitting: Recent Progress and Future Challenges. *J. Phys. Chem. Lett.* **2010**, *1*, 2655−2661.

(17) Murdoch, M.; Waterhouse, G. I. N.; Nadeem, M. A.; Metson, J. B.; Keane, M. A.; Howe, R. F.; Llorca, J.; Idriss, H. The Effect of Gold Loading and Particle Size on Photocatalytic Hydrogen Production from Ethanol over Au/TiO_2 Nanoparticles. *Nat. Chem.* **2011**, *3*, 489−492.

(18) Ni, M.; Leung, M. K. H.; Leung, D. Y. C.; Sumathy, K. A Review and Recent Developments in Photocatalytic Water-Splitting Using TiO_2 for Hydrogen Production. *Renewable Sustainable Energy Rev.* **2007**, *11*, 401−425.

(19) Yao, Y.; Li, G.; Ciston, S.; Lueptow, R. M.; Gray, K. A. Photoreactive TiO_2/Carbon Nanotube Composites: Synthesis and Reactivity. *Environ. Sci. Technol.* **2008**, *42*, 4952−4957.

(20) Zheng, Q.; Zhou, B. X.; Bai, J.; Li, L. H.; Jin, Z. J.; Zhang, J. L.; Li, J. H.; Liu, Y. B.; Cai, W. M.; Zhu, X. Y. Self-Organized TiO_2 Nanotube Array Sensor for the Determination of Chemical Oxygen Demand. *Adv. Mater.* **2008**, *20*, 1044−1049.

(21) Chen, H. M.; Chen, C. K.; Liu, R. S.; Zhang, L.; Zhang, J. J.; Wilkinson, D. P. Nano-Architecture and Material Designs for Water Splitting Photoelectrodes. *Chem. Soc. Rev.* **2012**, *41*, 5654−5671.

(22) Fujishima, A.; Honda, K. Electrochemical Photolysis of Water at a Semiconductor Electrode. *Nature* **1972**, *238*, 37−38.

(23) Nowotny, J.; Sorrell, C. C.; Sheppard, L. R.; Bak, T. Solar-Hydrogen: Environmentally Safe Fuel for the Future. *Int. J. Hydrogen Energy* **2005**, *30*, 521−544.

(24) Minggu, L. J.; Daud, W. R. W.; Kassim, M. B. An Overview of Photocells and Photoreactors for Photoelectrochemical Water Splitting. *Int. J. Hydrogen Energy* **2010**, *35*, 5233−5244.

(25) Reece, S.; Hamel, J. A.; Sung, K.; Jarvi, T. D.; Esswein, A. J.; Pijpers, J. J. H.; Nocera, D. G. Wireless Solar Water Splitting Using Silicon-Based Semiconductors and Earth-Abundant Catalysts. *Science* **2011**, *334*, 645−648.

(26) Hou, Y. D.; Abrams, B. L.; Vesborg, P. C. K.; Bjorketun, M. E.; Herbst, K.; Bech, L.; Setti, A. M.; Damsgaard, C. D.; Pedersen, T.; Hansen, O.; Rossmeisl, J.; Dahl, S.; Norskov, J. K.; Chorkendorff, I. Bioinspired Molecular Co-catalysts Bonded to a Silicon Photocathode for Solar Hydrogen Evolution. *Nat. Mater.* **2011**, *10*, 434−438.

(27) Selli, E.; L, C. G.; Quartarone, E.; Mustarelli, P.; I, R.; Fornia, L. A Photocatalytic Water Splitting Device for Separate Hydrogen and Oxygen Evolution. *Chem. Commun.* **2007**, *47*, 5022−5024.

(28) Brunauer, S.; Emmett, P. H.; Teller, E. Adsorption of Gases in Multimolecular Layers. *J. Am. Chem. Soc.* **1938**, *60*, 309−319.

(29) Barrett, E. P.; Joyner, L. G.; Halenda, P. P. The Determination of Pore Volume and Area Distributions in Porous Substances. I. Computations from Nitrogen Isotherms. *J. Am. Chem. Soc.* **1951**, *73*, 373−380.

(30) Zhang, W. F.; He, Y. L.; Zhang, M. S.; Yin, Z.; Chen, Q. Raman Scattering Study on Anatase TiO_2 Nanocrystals. *J. Phys. D: Appl. Phys.* **2000**, *33*, 912−916.

(31) Gomez-Navarro, C.; Weitz, R. T.; Bittner, A. M.; Scolari, M.; Mews, A.; Burghard, M.; Kern, K. Electronic Transport Properties of Individual Chemically Reduced Graphene Oxide Sheets. *Nano Lett.* **2007**, *7*, 3499−3503.

(32) Li, X. H.; Kurasch, S.; Kaiser, U.; Antonietti, M. Synthesis of Monolayer-Patched Graphene from Glucose. *Angew. Chem., Int. Ed.* **2012**, *51*, 9689−9692.

(33) Zhang, Y. H.; Tang, Z. R.; Fu, X. Z.; Xu, Y. J. TiO_2-Graphene Nanocomposites for Gas-Phase Photocatalytic Degradation of Volatile Aromatic Pollutant: Is TiO_2-Graphene Truly Different from Other TiO_2-Carbon Composite Materials? *ACS Nano* **2010**, *4*, 7303−7314.

(34) Liao, L. B.; Zhang, Q. H.; Su, Z. H.; Zhao, Z. Z.; Wang, Y. N.; Li, Y.; Lu, X. X.; Wei, D. G.; Feng, G. Y.; Yu, Q. K.; Cai, X. J.; Zhao, J. M.; Ren, Z. F.; Fang, H.; Robles-Hernandez, F.; Baldelli, S.; Bao, J. M. Efficient Solar Water-Splitting Using a Nanocrystalline CoO Photocatalyst. *Nat. Nanotechnol.* **2014**, *9*, 69−73.

(35) Mizoguchi, H.; Kamiya, T.; Matsuishi, S.; Hosono, H. A Germanate Transparent Conductive Oxide. *Nat. Commun.* **2011**, *2*, 470.

(36) Sakthivel, S.; Kisch, H. Daylight Photocatalysis by Carbon-Modified Titanium Dioxide. *Angew. Chem., Int. Ed.* **2003**, *42*, 4908−4911.

(37) Tauc, J.; Grigorov, R.; Vancu, A. Optical Properties and Electronic Structure of Amorphous Germanium. *Phys. Status Solidi B* **1966**, *15*, 627−637.

(38) Tang, H.; Prasad, K.; Sanjines, R.; Schmid, P. E.; Levy, F. Electrical and Optical-Properties of TiO_2 Anatase Thin-Films. *J. Appl. Phys.* **1994**, *75*, 2042−2047.

(39) Kang, Q.; Cao, J.; Zhang, Y.; L, L.; Xu, H.; Ye, J. Reduced TiO_2 Nanotube Arrays for Photoelectrochemical Water Splitting. *J. Mater. Chem. A* **2013**, *1*, 5766−5774.

(40) Wang, P.; Dimitrijevic, N. M.; Chang, A. Y.; Schaller, R. D.; Liu, Y.; Rajh, T.; Rozhkova, E. A. Photoinduced Electron Transfer Pathways in Hydrogen-Evolving Reduced Graphene Oxide-Boosted Hybrid Nano-Bio Catalyst. *ACS Nano* **2014**, *8*, 7995−8002.

(41) Li, Z.; Yao, C.; Yu, Y.; Cai, Z.; Wang, X. Highly Efficient Capillary Photoelectrochemical Water Splitting Using Cellulose Nanofiber-Templated TiO_2 Photoanode. *Adv. Mater.* **2014**, *26*, 2262−2267.

(42) Zhang, X.; Liu, Y.; Lee, S.-T.; Yang, S.; Kang, Z. Coupling Surface Plasmon Resonance of Gold Nanoparticles with Slow-Photon-Effect of TiO_2 Photonic Crystals for Synergistically Enhanced Photoelectrochemical Water Splitting. *Energy Environ. Sci.* **2014**, *7*, 1409−1419.

(43) Kim, T. W.; Choi, K. S. Nanoporous $BiVO_4$ Photoanodes with Dual-Layer Oxygen Evolution Catalysts for Solar Water Splitting. *Science* **2014**, *343*, 990−994.

(44) Hou, Y.; Zuo, F.; Dagg, A.; Feng, P. Visible Light-Driven α-Fe_2O_3 Nanorod/Graphene/$BiV_{1-x}Mo_xO_4$ Core/Shell Heterojunction Array for Efficient Photoelectrochemical Water Splitting. *Nano Lett.* **2012**, *12*, 6464−6473.

(45) Park, Y.; McDonald, K. J.; Choi, K. S. Progress in Bismuth Vanadate Photoanodes for Use in Solar Water Oxidation. *Chem. Soc. Rev.* **2013**, *42*, 2321−2337.

(46) Zou, Z.; Ye, J.; Sayama, K.; Arakawa, H. Direct Splitting of Water Under Visible Light Irradiation with an Oxide Semiconductor Photocatalyst. *Nature* **2001**, *414*, 625−627.

Supporting Information

Nano-Photoelectrochemical Cell Arrays with Spatially Isolated Oxidation and Reduction Channels

Hang-Ah Park,[†] Siyuan Liu,[†] Youngseok Oh, Paul A. Salvador, Gregory S. Rohrer, and

Mohammad F. Islam*

Department of Materials Science and Engineering, Carnegie Mellon University, 5000 Forbes

Avenue, Pittsburgh, Pennsylvania 15213-3890, United States

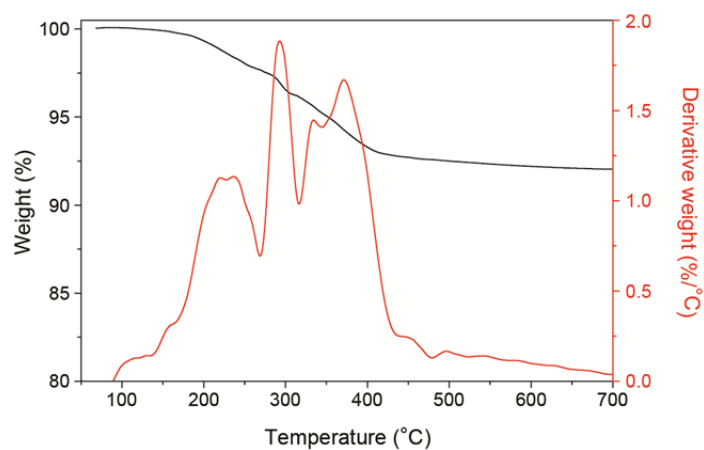[†]These authors contributed equally.

*E-mail: mohammad@cmu.edu.

Figure S1. Thermal gravimetric analysis (TGA) of TiO$_2$/CNT membrane under atmospheric air. The weight loss and the rate of weight loss (*i.e.,* derivative weight) *versus* temperature are associated with CNTs burning off from TiO$_2$/CNT membranes, providing the TiO$_2$:CNT mass ratio to be 92:8.
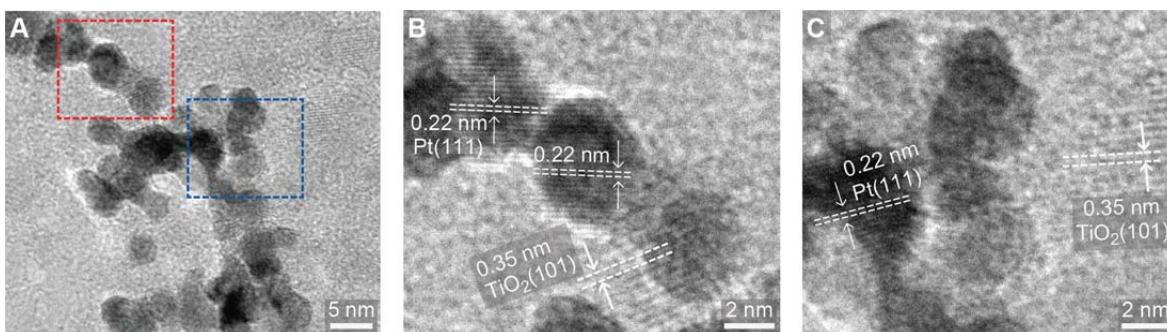
Figure S2. (A) High-resolution TEM image of TiO_2/CNT/Pt membranes to show TiO_2 and Pt nanoparticles. Region enclosed by red and blue rectangular boxes are magnified and shown in (B) and (C), respectively, to indicate lattice spacing of anatase TiO_2 and Pt nanoparticles. The lattice spacing of light grey particles is ~0.35 nm, which is similar to that of TiO_2 (101). The darker particles, on the other hand, have a lattice spacing of ~0.22 nm that matched well with Pt (111).
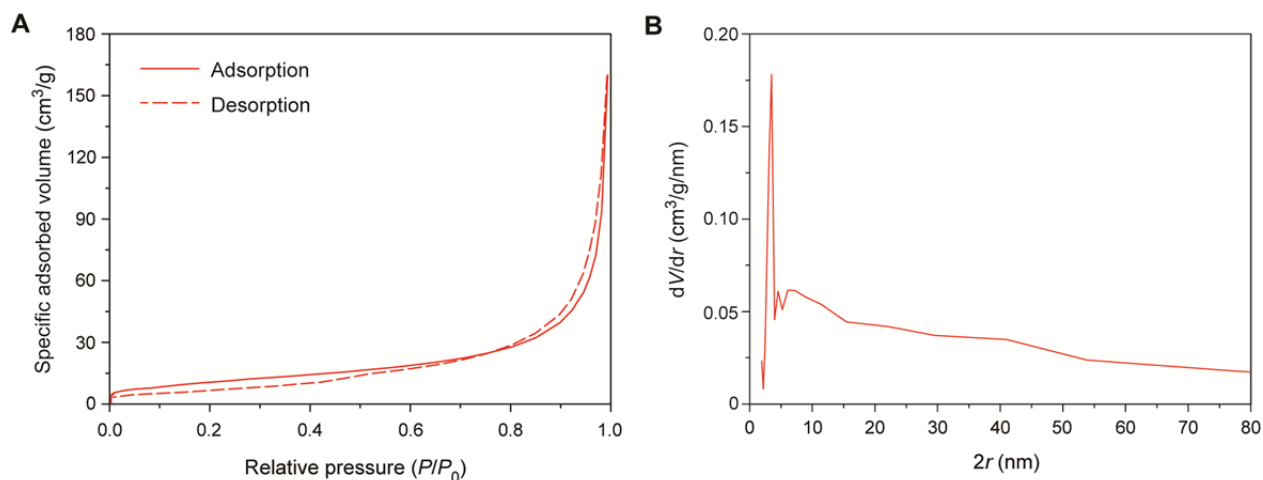
Figure S3. Adsorption isotherms and pore characteristics of TiO$_2$/CNT membranes. (A) Nitrogen adsorption–desorption isotherm of the membranes with a mass density ~43 mg/mL. Specific adsorbed volume, calculated by dividing measured adsorbed volume by mass of the sample, is plotted against relative pressure, P/P_0. Here, P and P_0 are equilibrium pressure and saturation pressure of nitrogen at the adsorption temperature of 77 K, respectively. (B) Pore diameter distribution (dV/dr) *versus* pore diameter ($2r$) of the membranes.
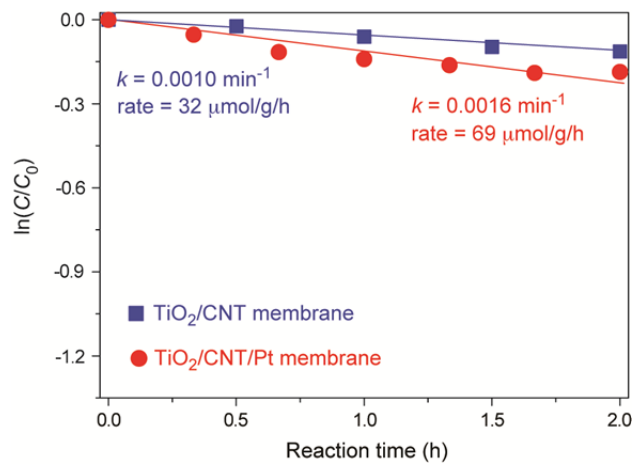
Figure S4. Adsorption–desorption equilibration time of methylene blue dye on TiO_2/CNT/Pt and TiO_2/CNT membranes in the dark.
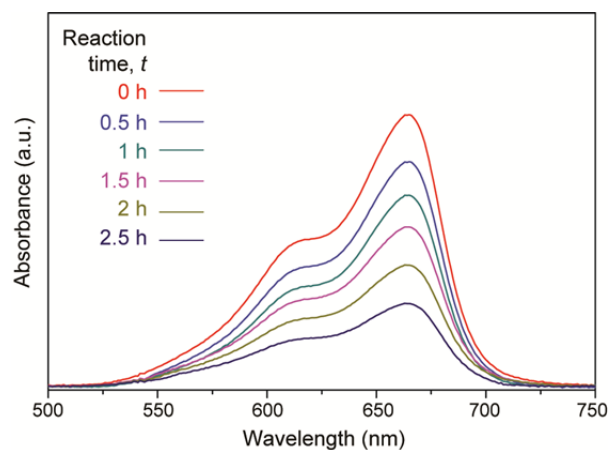
Figure S5. Absorption spectra at reaction time (*t*) intervals of 0.5 h from a methylene blue dye solution containing the nano-PEC arrays after dye adsorption equilibration and under visible-light irradiation. Dye concentration *C* was determined from absorbance at 665 nm.
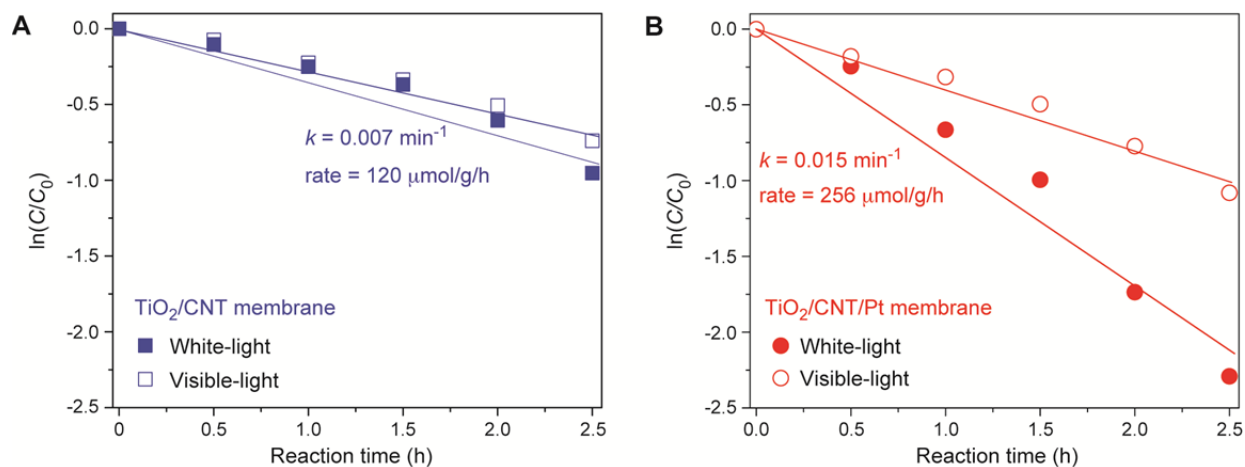
Figure S6. Photocatalytic methylene blue dye degradation of (A) TiO$_2$/CNT membrane and (B) TiO$_2$/CNT/Pt membrane under white-light and visible-light. The degradation rate and k are under white-light only. These rates and k under visible-light irradiation are in Figure 6A.
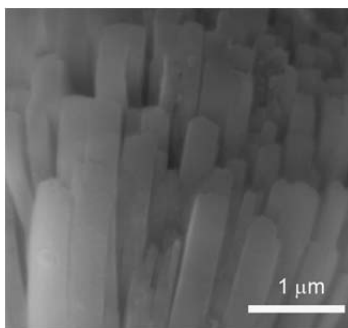
Figure S7. An SEM image of TiO$_2$/CNT/Pt nanotubes after being soaked in PVA polymer solution shows that PVA fills all the nanotubes. An SEM image of the same nanotubes before being filled with PVA is shown in Figure 2A.
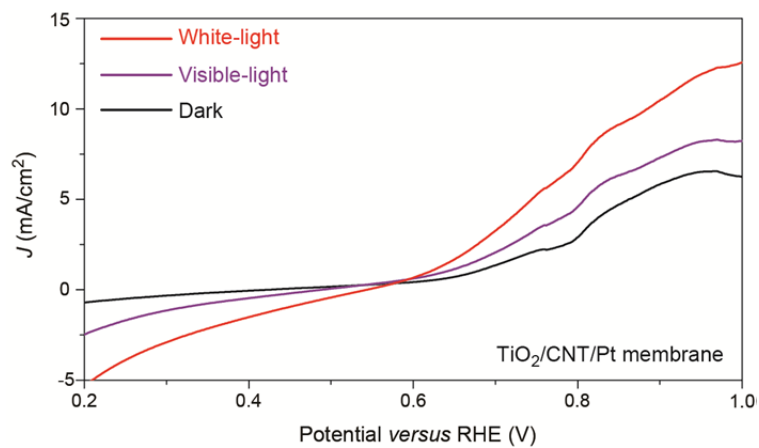
Figure S8. The representative *J–V* curves of TiO$_2$/CNT/Pt membrane on the RHE scale.
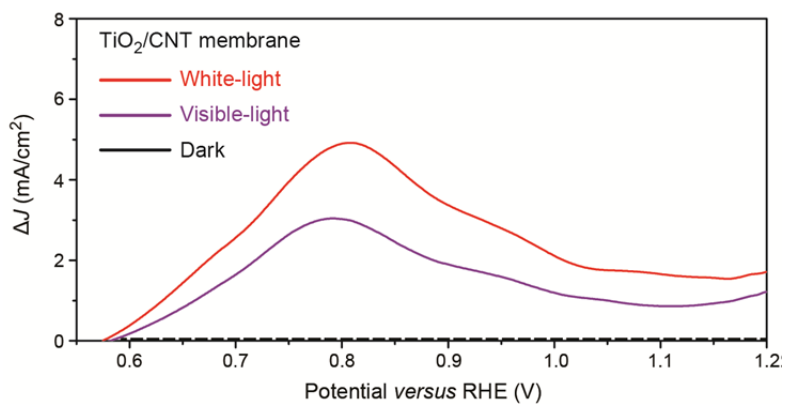
Figure S9. The photogenerated current density *versus* potential (ΔJ–V) curves on a RHE scale for TiO$_2$/CNT membranes under white- and visible-light in 1 M Na$_2$SO$_4$ electrolytes at pH 5.9.
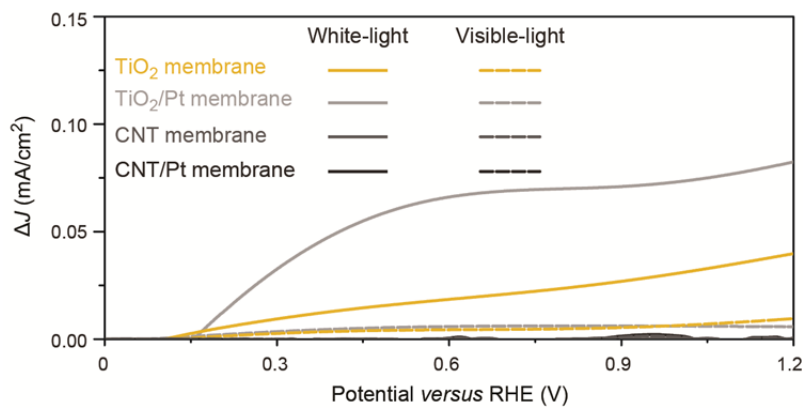
Figure S10. ΔJ–V curves on a RHE scale by TiO_2, TiO_2/Pt, CNT, CNT/Pt membranes under white- and visible-light in 1 M Na_2SO_4 electrolytes at pH 5.9.
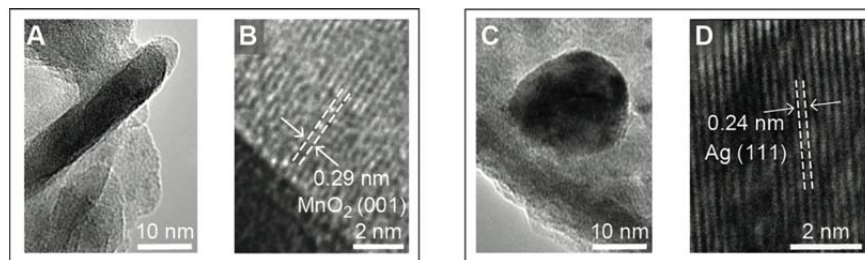
Figure S11. TEM images of MnO_x flakes and Ag nanoparticles on the outer wall surface and in the inside of TiO_2/CNT/Pt nanotubes, respectively. (A) MnO_x flakes are easily distinguishable conventional resolution TEM images due to their distinct shapes. (B) A lattice parameter of 0.29 nm, obtained from high Resolution TEM images of MnO_x flakes, matches well with the lattice spacing of MnO_2 (001) plane. (C) Conventional-resolution TEM images show Ag nanoparticles of diameter 20 nm are predominantly located in the inside of the nanotubes. (D) A lattice parameter of 0.24 nm, obtained from high-resolution TEM images, is consistent with the lattice spacing of Ag (111) plane.
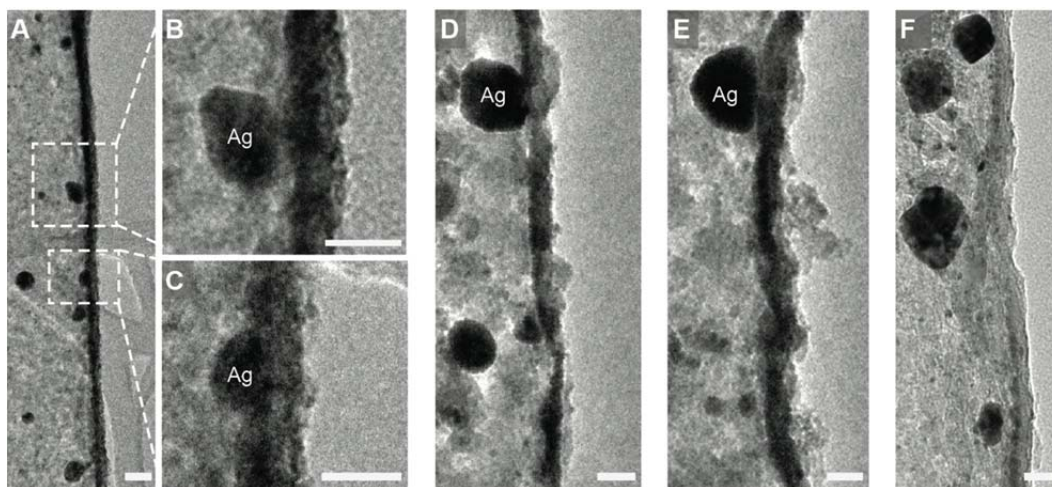
Figure S12. (A-F) Conventional resolution TEM images show photodeposited Ag nanoparticles particles on the interior CNT wall of TiO$_2$/CNT/Pt membranes near or next to Pt nanoparticles. Scale bars = 20 nm.

Table S1. Comparison of photocatalytic dye degradation performance by various photocatalysts.

Photocatalysts	Light source, power, spectral range	Dye:photocatalyst molar ratio[a]	Degradation rate[a] [μmol/g/h]	Rate constant[a] (k) [min^{-1}]	reference
TiO$_2$/CNT/Pt membrane	Hg, 300 W, white	0.12	256	0.015	this work
	Hg, 300 W, visible		140	0.007	
TiO$_2$/CNT membrane	Hg, 300 W, visible		120	0.007	
	Hg, 300 W, visible		110	0.005	
TiO$_2$/SWCNT aerogels	Hg, 300 W, visible	0.004	25	0.012	ref 1
ZnWO$_4$/graphene	Xe, 500 W, visible	0.006	7.7	0.008	ref 2
TiO$_{2-x}$/graphene	W, 450W, visible	0.005	9.5	0.0045	ref 3
TiO$_2$/N-doped MWCNT	Xe, 450 W, visible	N.A.[b]	N.A.[b]	0.014	ref 4
P25/graphene	Xe, 500 W, visible	0.003	23.6	0.018	ref 5
TiO$_2$/carbon-dot	Xe, 1000 W, visible	0.012	5.1	0.0047	ref 6
ZnIn$_2$S$_4$	Xe, 500 W, visible	0.026[c]	29.3	0.011	ref 7
TiO$_2$/MWCNT	N.A., 125 W, white	0.006[d]	102	0.080	ref 8

[a]After dye adsorption to the samples had reached equilibrium in the dark.

[b]Used thin film of dimensions 0.8 cm × 0.8 cm. Sample masses were not reported.

[c]Used methyl orange dye.

[d]Used reactive orange 16 dye.

Table S2. Comparison of photocurrent generated by various photocatalysts.

Photocatalysts	Electrolyte	Illumination power density [mW/cm^2], spectral range	Scan rate [mV/s]	Maximum ABPE [%]	Photocurrent at maximum ABPE [mA/cm^2]	reference
TiO$_2$/CNT/Pt membrane	1 M Na$_2$SO$_4$	100, white	10	1.8	4.2	this work
		73, visible		1.0	1.7	
Reduced TiO$_2$ nanotubes	1 M NaOH	100, AM 1.5 G	10	1.3	0.73	ref 9
TiO$_2$/RGO	0.1 M Na$_2$SO$_4$	120, white	20	-	0.078	ref 10
Cellulose-templated TiO$_2$	1 M KOH	100, white	-	0.85	0.95	ref 11
Au/TiO$_2$	1 M KOH	100, AM 1.5 G	50	0.71	1.35	ref 12
Fe$_2$O$_3$/RGO/ BiV$_{1-x}$Mo$_x$O$_4$	0.01 M Na$_2$SO$_4$	100, AM 1.5 G	-	0.53	0.75	ref 13
BiVO$_4$/FeOOH /NiOOH	0.5 M KH$_2$PO$_4$ + 1 M Na$_2$SO$_3$	100, AM 1.5 G	10	1.75	2.70	ref 14

References

1.   Park, H.-A.; Liu, S.; Salvador, P. A.; Rohrer, G. S.; Islam, M. F. High Visible-Light Photochemical Activity of Titania Decorated on Single-Wall Carbon Nanotube Aerogels. *RSC Adv.* **2016**, 6, 22285-22294.

2.   Bai, X. J.; Wang, L.; Zhu, Y. F. Visible Photocatalytic Activity Enhancement of $ZnWO_4$ by Graphene Hybridization. *ACS Catal.* **2012**, 2, 2769-2778.

3.   Xing, M.; Li, X.; Zhang, J. Synergistic Effect on the Visible Light Activity of Ti^{3+} Doped TiO_2 Nanorods/Boron Doped Graphene Composite. *Sci. Rep.* **2014**, 4, 5493.

4.   Lee, W. J.; Lee, J. M.; Kochuveedu, S. T.; Han, T. H.; Jeong, H. Y.; Park, M.; Yun, J. M.; Kwon, J.; No, K.; Kim, D. H.; Kim, S. O. Biomineralized N-doped CNT/TiO_2 Core/Shell Nanowires for Visible Light Photocatalysis. *ACS Nano* **2012**, 6, 935-943.

5.   Zhang, H.; Lv, X. J.; Li, Y. M.; Wang, Y.; Li, J. H. P25-Graphene Composite as a High Performance Photocatalyst. *ACS Nano* **2010**, 4, 380-386.

6.   Cui, G. W.; Wang, W. L.; Ma, M. Y.; Zhang, M.; Xia, X. Y.; Han, F. Y.; Shi, X. F.; Zhao, Y. Q.; Dong, Y. B.; Tang, B. Rational Design of Carbon and TiO_2 Assembly Materials: Covered or Strewn, Which is Better for Photocatalysis? *Chem. Commun.* **2013**, 49, 6415-6417.

7.   Chen, Z.; Li, D.; Zhan, W.; Shao, Y.; Chen, T.; Sun, M.; Fu, X. Photocatalytic Degradation of Dyes by $ZnIn_2S_4$ Microspheres Under Visible Light Irradiation. *J. Phys. Chem. C* **2009**, 113, 4433-4440.

8.   Djokic, V. R.; Marinkovic, A. D.; Ersen, O.; Uskokovic, P. S.; Petrovic, R. D.; Radmilovic, V. L. R.; Janackovic, D. T. The Dependence of the Photocatalytic Activity of TiO_2/Carbon Nanotubes Nanocomposites on the Modification of the Carbon Nanotubes. *Ceram. Int.* **2014**, 40, 4009-4018.

9.   Kang, Q.; Cao, J.; Zhang, Y.; L, L.; Xu, H.; Ye, J. Reduced TiO_2 Nanotube Arrays for Photoelectrochemical Water Splitting. *J. Mater. Chem. A* **2013**, 1, 5766-5774.

10.   Wang, P.; Dimitrijevic, N. M.; Chang, A. Y.; Schaller, R. D.; Liu, Y.; Rajh, T.; Rozhkova, E. A. Photoinduced Electron Transfer Pathways in Hydrogen-Evolving Reduced Graphene Oxide-Boosted Hybrid Nano-Bio Catalyst. *ACS Nano* **2014**, 8, 7995-8002.

11.   Li, Z.; Yao, C.; Yu, Y.; Cai, Z.; Wang, X. Highly Efficient Capillary Photoelectrochemical Water Splitting Using Cellulose Nanofiber-Templated TiO_2 Photoanode. *Adv. Mater.* **2014**, 26, 2262-2267.

12.   Zhang, X.; Liu, Y.; Lee, S.-T.; Yang, S.; Kang, Z. Coupling Surface Plasmon Resonance of Gold Nanoparticles with Slow-Photon-Effect of TiO_2 Photonic Crystals for Synergistically Enhanced Photoelectrochemical Water Splitting. *Energy Environ. Sci.* **2014**, 7, 1409-1419.

13.   Hou, Y.; Zuo, F.; Dagg, A.; Feng, P. Visible Light-Driven α-Fe_2O_3 Nanorod/Graphene/$BiV_{1-x}Mo_xO_4$ Core/Shell Heterojunction Array for Efficient Photoelectrochemical Water Splitting. *Nano Lett.* **2012**, 12, 6464-6473.

14.   Kim, T. W.; Choi, K. S. Nanoporous $BiVO_4$ Photoanodes with Dual-Layer Oxygen Evolution Catalysts for Solar Water Splitting. *Science* **2014**, 343, 990–994.